KeAi
CHINESE ROOTS
GLOBAL IMPACT

Available online at www.keaipublishing.com/en/journals/journal-of-magnesium-and-alloys/

ScienceDirect

Journal of Magnesium and Alloys 22 (2026) 102189

www.elsevier.com/locate/jma

Full Length Article

Defect-suppressed extrusion of high-purity magnesium: A processing–structure–defect framework for biodegradable implants

Weichao Li, Degang Xie*, Tingjiang Pan, Chuanwei Fan, Fengge Xi, Yuanhao Jia, Zhiwei Shan*

Engineering Research Center for Magnesium-based New Materials, Center for Advancing Materials Performance from the Nanoscale (CAMP-Nano), State Key Laboratory for Mechanical Behavior of Materials, Xi'an Jiaotong University, Xi'an 710049, China

Received 8 April 2026; received in revised form 11 June 2026; accepted 14 June 2026
Available online 9 July 2026

Abstract

High-purity magnesium is an attractive platform for biodegradable implants because it minimizes risks associated with alloying elements, yet its clinical translation is constrained by poor hot workability and the persistence of casting-derived defects that accelerate mechanical failure and corrosion. Here we establish a processing-structure-defect framework that enables defect-suppressed extrusion of 4N(99.99 wt.%) Mg into rods with structural characteristics relevant to biodegradable implant applications. Processing maps derived from hot-compression experiments and Arrhenius-type constitutive modelling reveal an unusually narrow stability window governed by low strain-rate sensitivity and limited dynamic recrystallization in coarse-grained pure Mg. Guided by this map, low-strain-rate extrusion within dynamic recovery/recrystallization-stable domains promotes pore collapse and spheroidization while avoiding flow instability. As a result, the maximum defect size is reduced to < 60 μm, nearly two orders of magnitude smaller than in commercial high-purity Mg rods. The refined defect state translates into a tensile strength above 190 MPa and an *in vitro* degradation rate of ~0.2 mm·year^{-1}, demonstrating that mechanical integrity and corrosion control can be achieved simultaneously in high-purity Mg. This work therefore offers a scalable and practically accessible route to manufacturing defect-controlled pure Mg rods with structural and degradation characteristics relevant to biodegradable implant applications.
© 2026 Chongqing University. Publishing services provided by Elsevier B.V. on behalf of KeAi Communications Co. Ltd.
This is an open access article under the CC BY-NC-ND license (http://creativecommons.org/licenses/by-nc-nd/4.0/)

Keywords: High-purity magnesium; Hot deformation; Defect control; Biodegradable magnesium.

1. Introduction

Magnesium (Mg) has emerged as a promising material for next-generation biodegradable medical implants, owing to its unique combination of mechanical compatibility with bone, intrinsic biodegradability, and outstanding biocompatibility [1,2]. Unlike inert metals such as titanium or cobalt–chromium alloys, Mg–based implants can sustain physiological loads while gradually resorbing *in vivo* [3], thereby eliminating the need for secondary removal surgeries [4]. To date, most biodegradable devices have been based on Mg alloys [5] (e.g., Mg–RE, Mg–Zn, and Mg–Ca), exemplified by the clinically approved Magmaris® coronary scaffold [6]. However, high–purity Mg (> 99.99 wt.%) offers inherent biosafety advantages, as alloying elements released during degradation may provoke adverse biological responses, whereas pure Mg largely avoids these risks. Accordingly, several high–purity Mg devices—including the NOVAMag® membrane [7], a degradable closing clip [8] (Suzhou Origin Medical Technology Co., Ltd., China), and high–purity Mg screws [9] (Eon Technology Co., Ltd., China)—have recently received regulatory approval, underscoring a growing preference for pure Mg when mechanical performance permits.

For orthopedic and dental applications, Mg rods [10,11] serve as versatile feedstock for screws [12–14], narrow bone plates [15], and nails [16], and must meet stringent requirements [17,18]: ultra–high chemical purity [19–22], extremely low porosity and inclusion content [23–25], a uniform grain structure, reliable mechanical properties and appropriate degradation rate under physiological conditions. Defects such as pores and non–metallic inclusions are especially detri-

Peer review under the responsibility of Chongqing University.
* Corresponding authors.
E-mail addresses: dg_xie@xjtu.edu.cn (D. Xie), zwshan@xjtu.edu.cn (Z. Shan).

https://doi.org/10.1016/j.jma.2026.102189
2213-9567/© 2026 Chongqing University. Publishing services provided by Elsevier B.V. on behalf of KeAi Communications Co. Ltd. This is an open access article under the CC BY-NC-ND license (http://creativecommons.org/licenses/by-nc-nd/4.0/)

mental, acting as stress concentrators that reduce the effective load–bearing cross–section, degrade tensile and fatigue strength, and accelerate localized corrosion [26–30]. In implants with characteristic dimensions of only a few millimeters [31], even sub–millimeter defects can critically compromise mechanical properties. For instance, increasing porosity from 0.07% to 4.06% lowers the fatigue limit from 82 to 32 MPa [32], while reducing pore size from ∼110 to ∼80 μm roughly doubles fatigue life [33]. Proposed specifications for wrought biomedical rods (GB/T 6519–2024) require that no defect exceeds 0.4 mm; for orthopedic applications, defect–tolerance analyses suggest a more stringent limit of < 100 μm and a total defect volume fraction < 0.03 vol.% to ensure both mechanical integrity and controlled biodegradation. Moreover, defect size, morphology and spatial distribution are critical to corrosion susceptibility, film stability and degradation uniformity, particularly when defects intersect the surface or become exposed during corrosion. Defect-containing rods can exhibit faster and more non-uniform corrosion than dense counterparts [34–35], as corrosion initiation at these defect sites can promote repeated film rupture and reformation, thereby accelerating localized degradation [36]. Nevertheless, commercial Mg rods face quality challenges beyond compositional variability, with inclusions and pores representing the more critical concern for implant-grade feedstocks. Indeed, the examined commercial high-purity Mg rod was found to contain inclusions or pores as large as ∼1.5 mm, far exceeding acceptable limits for small biodegradable implants. Consequently, downstream manufacturers often have to perform piece-by-piece non-destructive inspection before machining purchased rods into medical devices, indicating that defect management still relies heavily on post-production screening rather than systematic control at the feedstock and processing stages.

Such defect-related limitations are rooted in the coupling between casting quality and subsequent thermomechanical processing [37,38]. During casting, non-uniform temperature fields, variable cooling rates, solidification shrinkage and melt oxidation can introduce pores and inclusion clusters [39]. These inherited defects are not fixed features: during extrusion, they may either close and spheroidize under stable compressive flow or elongate and propagate under unstable deformation. Therefore, extrusion temperature, strain rate, cooling rate and thermal exposure jointly determine both microstructure evolution [40–44] and defect evolution [45,46]. This coupling is particularly critical for pure Mg. Pure Mg contains minimal solute, resulting in large as-cast grain sizes, sluggish dynamic recrystallization(DRX), and limited activation of non-basal slip systems [47,48]. These factors reduce deformation homogeneity, increase susceptibility to cracking at low temperatures, and promote flow instability [49–51], making defect closure highly sensitive to the imposed deformation path. Consequently, achieving defect–suppressed extrusion of high–purity Mg requires a comprehensive understanding of its thermomechanical behavior and the conditions that favor defect closure over propagation.

In this work, we establish a processing–structure–defect framework that enables defect–suppressed extrusion of 4N(99.99 wt.%) Mg into rods with structural characteristics relevant to biodegradable implant applications. We begin with high–quality billets produced by a controlled thin–layer solidification casting(CTLSC) route developed by our team [52], which minimizes casting–derived defects. The hot deformation behavior is systematically investigated via Gleeble hot–compression experiments across a range of temperatures and strain rates. Using the Dynamic Material Model(DMM) and an Arrhenius–type constitutive analysis, we construct processing maps that reveal an unusually narrow stability window for coarse–grained pure Mg, governed by low strain–rate sensitivity and limited dynamic recrystallization. Guided by these maps, we perform extrusion trials within the dynamic recovery(DRV)/DRX–stable domain, promoting pore collapse and spheroidization while avoiding flow instability. The resulting rods exhibit a maximum defect size below 60 μm, nearly two orders of magnitude smaller than commercial high–purity Mg rods, and achieve a tensile strength exceeding 190 MPa together with an *in vitro* degradation rate of ∼0.2 mm·year^{-1} in Hank's solution. This work therefore provides a practical route to defect-controlled pure Mg rods with structural and degradation characteristics relevant to biodegradable implant applications, with broader implications for the processing of high-purity Mg and Mg alloys.

2. Methods

2.1. Sample preparation and characterization

The microstructure of the high-purity Mg consists predominantly of α-Mg, with a broad grain-size distribution ranging from ∼0.1 to 1.6 mm. The average grain size is approximately 500 μm, with maximum and minimum grain sizes of ∼1500 μm and ∼100 μm, respectively, as shown in Fig. 1. The chemical composition of the Mg was determined using a GNR S9 optical emission spectrometer, and the measured elemental contents are summarized in Table S1.

The extrusion billet was produced by closed-atmosphere induction melting followed by controlled thin-layer solidification casting. In CTLSC, Mg feedstock is melted under high-purity argon in a sealed furnace and the melt delivery rate is precisely regulated while passing through a flow-control and filtration stage, so that only small aliquots of liquid Mg are introduced into a preheated graphite mold, where they spread into a transient thin melt layer at the solidification front. This near-isothermal thin-layer solidification mode minimizes thermal gradients and feeding-related contraction, thereby suppressing macroscale segregation, shrinkage porosity and inclusion clustering, and producing dense billets suitable for subsequent extrusion.

Internal defects in the billet were characterized by X-ray computed tomography (CT) (Fig. 2). The overall porosity is low, at ∼0.6 vol.‰ (Fig. 2(a)). As shown in Fig. 2(b), defects larger than 350 μm are mainly located at the ingot bottom and near-subsurface regions, whereas smaller defects (< 350 μm) are more uniformly distributed within the interior (the semi-

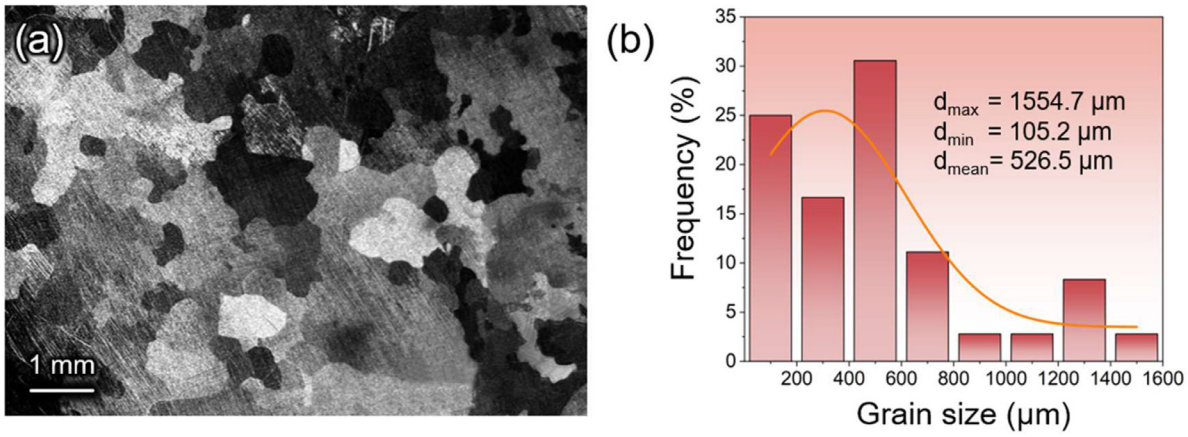


Fig. 1. Grain size and distribution of the as-cast 4N pure magnesium ingot. (a) Optical micrograph. (b) Statistical distribution.

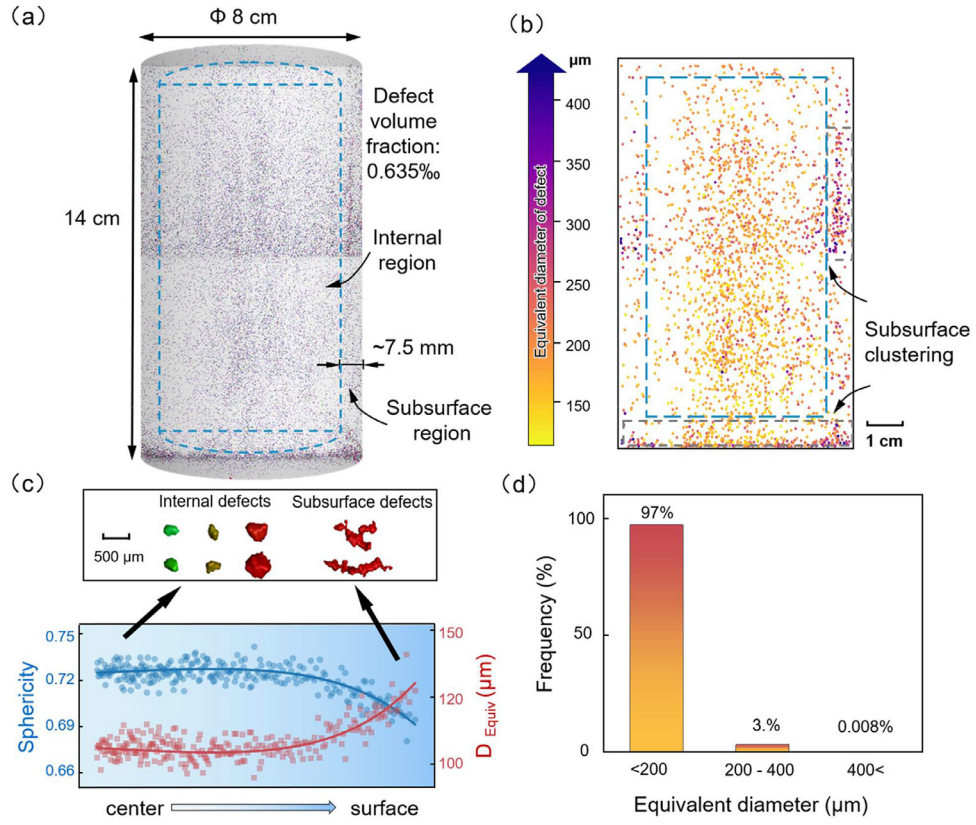


Fig. 2. Characterization of defect morphology and distribution in an as-cast 4N pure Mg ingot via CT analysis. (a) Three-dimensional reconstruction of the defect spatial distribution in the as-cast ingot. (b) Size distribution of defect in the ingot, showing the clustering of large defects at the subsurface region. (c) Variation of defect sphericity and equivalent diameter with distance from center. (d) Histogram showing the frequency of defect sizes in (b).

cylindrical region outlined by blue dashed lines in Fig. 2(a)). Representative examples are shown in Fig. 2(c): the largest defect is > 600 μm, while most smaller defects are equiaxed (more information was shown in Table S2). From the ingot center toward the near-surface region, defect size increases progressively, accompanied by a decrease in sphericity. Detailed statistical descriptors of defects morphology are provided in Table S2. The size distribution (Fig. 2(d)) shows that > 97% of defects are smaller than 200 μm, whereas defects larger than 400 μm account for only 0.008%.

2.2. Gleeble hot compression

The experiments were conducted on a Gleeble-3800 thermomechanical simulator for hot compression, using four deformation temperatures (150 °C, 200 °C, 250 °C, and 300 °C) and four strain rates (0.001 s^{-1}, 0.01 s^{-1}, 0.1 s^{-1}, and 1 s^{-1}) at each temperature. The height reduction of all samples was set to 40% (equivalent to a true strain of 0.51). Hot compression specimens were wire-cut directly from the as-cast Mg ingot, and the surfaces were polished with 1000-grit SiC paper to

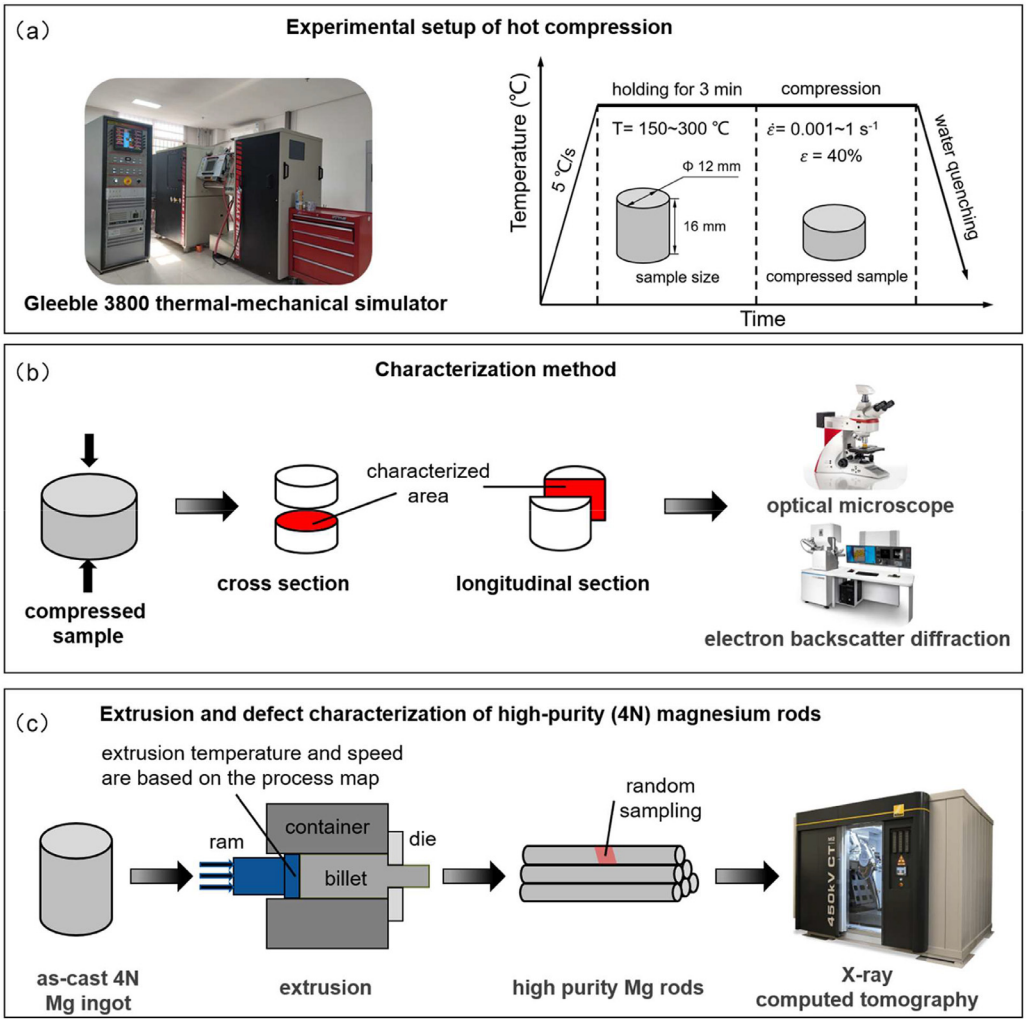


Fig. 3. Experimental setup and characterization procedure. (a) Experimental setup of hot compression. (b) Experimental procedure for metallographic characterization using optical microscope and EBSD. (c) Fabricating high-purity Mg rods by extrusion and characterization of internal defects by X-ray CT.

remove the oxidized layer; no pre-deformation heat treatment was applied. Specimens were heated to the target temperature at 5 °C/s and held for 3 min to achieve thermal equilibrium. Compression was then performed at the prescribed strain rate to the target strain. After compression the samples were removed and water-quenched (Fig. 3(a)).

After the hot compression experiments, all samples were sectioned, ground and polished for metallographic analysis. The sample surfaces were sequentially sanded with 400-, 800-, 1500-, 2500-, 5000-, and 7000-grit papers and polished with 0.25 μm alumina suspension to ensure a consistent surface condition. Microstructures (grain size, morphology and distribution) were examined using an optical microscope (Leica DM4M). For further characterization, selected specimens were prepared for EBSD (Fig. 3(b)).

2.3. Extrusion trials

Extrusion trials were conducted with pure Mg billets (Φ90 × 200 mm) on a horizontal 800-ton hydraulic press, producing rods of 10 mm diameter without lubrication. Prior to extrusion, these billets were machined to remove the surface layer and then soaked at a set temperature for 3 h to ensure thermal equilibration. The extrusion temperature and ram speed were selected from the processing map Fig. 4(e) by converting the prescribed temperature-strain-rate windows into machine-set parameters through Eq. (10); owing to equipment limitations, the lowest attainable strain rate was 0.04 s^{-1}. Post-extrusion specimens were cut and examined by X-ray computed tomography (AX-3000CT-D). Porosity metrics (volume fraction, size, and morphology) were quantified and compared with those of commercial pure Mg rods (Fig. 3(c)).

2.4. Immersion test

Corrosion performance was evaluated through controlled immersion experiments using Φ10 × 5 mm samples. The sample surfaces were sequentially sanded with 400-, 800-, 1500-, 2500-grit papers, with initial masses (m_i) recorded before immersion. The test was conducted in Hank's solution (Table S3) in accordance with JB/T 7901–2023, maintaining a 20 mL·cm^{-2} solution-to-surface area ratio at 37 °C. The

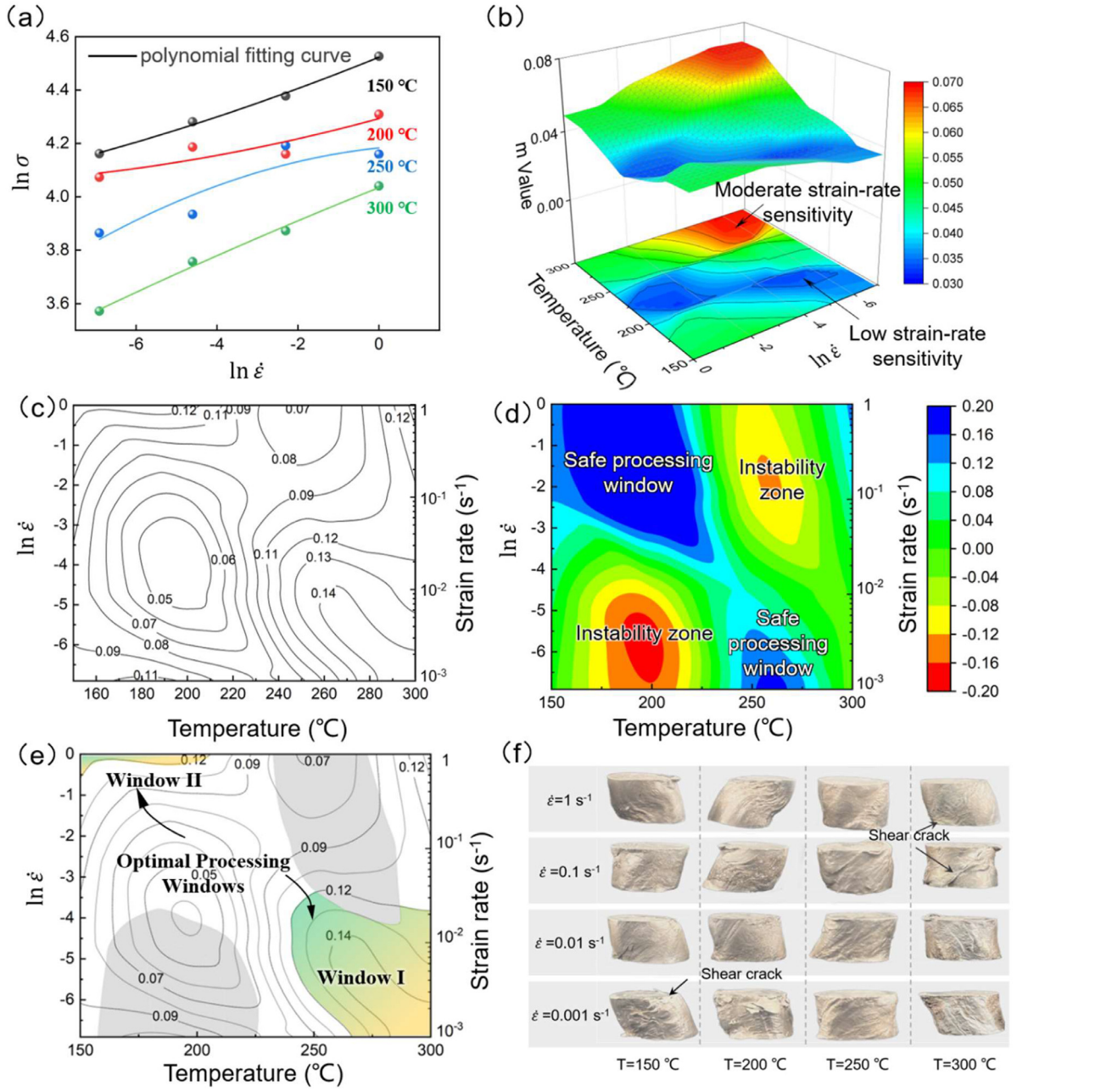


Fig. 4. Strain-rate-sensitivity-based processing maps of as-cast 4N-purity Mg at an engineering compressive strain of 0.40. (a) Polynomial fitting results of $\ln \sigma$ and $\ln \varepsilon$ for calculating the strain rate sensitivity factor (m). (b) Three-dimensional plot of m as a function of temperature and strain rate. (c) Power dissipation map. (d) Flow instability map. (e) Processing map obtained by superimposing power-dissipation and instability domains to reveal the optimal processing windows. (f) Morphology of the compressed specimens.

immersion duration was set to 1 week, with hydrogen evolution measured intermittently throughout the period. Three replicate specimens were tested for each condition. After immersion, samples were rinsed with deionized water, dried with ethanol and cleaned with Chromic acid (200 g·L^{-1} CrO_3 + 10 g·L^{-1} $AgNO_3$) before final mass measurements (m_f). The degradation rates were calculated using:

$$P_H = 2.279\frac{H_i - H_f}{At} \quad (1)$$

$$P_W = 2.100\frac{m_i - m_f}{At} \quad (2)$$

Here, P_H and P_W denote the corrosion rates determined from hydrogen evolution and weight loss measurements, respectively. H_i - H_f represents the net hydrogen evolution volume (mL). A is the exposed surface area (cm^2), and t is the immersion time (day).

2.5. Tensile test

Tensile tests were performed in accordance with GB/T 228.1–2021 standards to evaluate the mechanical properties of extruded rods. The tests were conducted at room temper-

ature using a universal testing machine (ETM105D), with a crosshead speed of 1 mm/min. The stress-strain data were recorded during the test, from which the ultimate tensile strength (σ), yield strength (σ_γ), and elongation (ε) were determined. To ensure repeatability and statistical reliability, three replicate specimens were tested.

3. Results

3.1. Processing map of 4N high-purity Mg

Representative true stress-strain curves (Fig. S1) demonstrate strong temperature- and strain-rate-dependent flow behavior in as-cast 4N Mg. At a high strain rate of 1 s^{-1}, the curves are dominated by rapid hardening with negligible post-peak softening, consistent with dislocation multiplication outpacing dynamic restoration. Reducing the strain rate to 0.1 s^{-1} introduces a clear peak stress followed by softening at 300 °C, whereas the curves at 150–250 °C evolve towards a near-steady plateau, indicating a transition from work hardening to DRV-controlled flow with DRX becoming discernible only at elevated temperature. At lower strain rates of 0.01–0.001 s^{-1}, the flow response between 250 and 300 °C becomes increasingly plateau-like with smooth steady flow, consistent with enhanced thermal activation that lowers the critical strain for DRX and suppresses twinning. In contrast, temperatures below 200 °C show sharp peaks with abrupt softening, accompanied by extensive $\{10\bar{1}2\}\langle 10\bar{1}1\rangle$ tensile twinning in the deformed microstructure, highlighting a twinning-dominated regime that limits dynamic restoration.

In studying the hot deformation behavior of metallic Mg, processing maps based on the Dynamic Material Model [53] (DMM) provide a better understanding of the relationship between plastic deformation and material energy dissipation. The power P absorbed per unit volume of the material can be expressed as follows:

$$P = G + J = \int_0^{\dot{\varepsilon}} \sigma d\dot{\varepsilon} + \int_0^{\sigma} \dot{\varepsilon} d\sigma \tag{3}$$

Here, G denotes the significant component of power dissipation in the elastic state, while J mainly represents the power dissipation during plastic flow and subsequent microstructural changes such as shear band development, crack nucleation, dynamic recrystallization, and dynamic recovery. The energy shares of G and J are related to the strain rate sensitivity index m, which can be interpreted as:

$$m = \frac{\partial J}{\partial G} = \frac{\dot{\varepsilon}\partial\sigma}{\sigma\partial\dot{\varepsilon}} = \frac{\partial \ln\sigma}{\partial \ln\dot{\varepsilon}} \tag{4}$$

As shown in Fig. 4(a), the peak stress extracted from each flow curve was used to determine the strain-rate sensitivity m (Table S4), yielding m = 0.03–0.08 across the investigated domain (Fig. 4(b)). The modest increase to 0.05–0.08 is confined to 250–300 °C and 10^{-3}–10^{-2} s^{-1}, whereas most conditions remain at $m < 0.05$. In Mg, such low m is commonly associated with deformation accommodated primarily by basal slip and twinning [54,55], while the slight increase at elevated temperature suggests partial participation of non-basal slip and cross-slip-assisted DRV, with limited DRX consistent with the flow-curve softening at 300 °C (Fig. S1).

The power dissipation factor η is expressed as:

$$\eta = \frac{J}{J_{\mathrm{Max}}} = \frac{2m}{1+m} \tag{5}$$

Generally, a higher η indicates that a larger fraction of the imposed power is dissipated through microstructural evolution (e.g., DRV and DRX), which is often beneficial for hot working. However, η alone does not guarantee stable plastic flow, and deformation localization (e.g., shear banding) may still occur under certain conditions. Accordingly, Prasad proposed a plastic (flow) instability criterion [56]:

$$\xi(\dot{\varepsilon}) = \frac{\partial \ln\left[\frac{m}{m+1}\right]}{\partial \ln\dot{\varepsilon}} + m < 0 \tag{6}$$

Following this methodology, we constructed the power dissipation map (Fig. 4(c)), instability map (Fig. 4(d)), and the superimposed processing map (Fig. 4(e)) for 4N high-purity Mg. Across 150–300 °C, the maximum power dissipation efficiency is only ~0.15, substantially below values typically associated with DRV (~0.20 to 0.30) and DRX (~0.35 to 0.45) in Mg alloys [57]. This low η indicates that coarse-grained high-purity Mg dissipates only a limited fraction of deformation power through microstructural evolution, and instead deforms predominantly through low-dissipation mechanisms. The unusually low η is consistent with (i) limited solute-assisted strengthening in pure Mg, which constrains the activation of <c+a> slip even above ~225 °C, and (ii) a coarse initial grain size that raises the critical strain for DRX initiation.

Fig. 4(d) shows a bipolar distribution of the instability factor, with unstable domains located at both low temperature/low strain rate (150–200 °C, 0.001–0.018 s^{-1}) and high temperature/high strain rate (260–300 °C, 0.018–1.00 s^{-1}). The low-temperature instability is consistent with restricted activation of non-basal systems in HCP Mg, promoting strain localization when deformation is accommodated mainly by basal slip and twinning. Conversely, the high-temperature/high-rate instability is consistent with adiabatic heating and local softening, which can trigger shear localization and cracking.

Superimposing the dissipation and instability maps (Fig. 4(e)) identifies two stable regions with η ~0.12 to 0.14: region I (150–210 °C/0.36–1.00 s^{-1}) and region II (253–283 °C/0.001–0.01 s^{-1}). Although both satisfy the stability criterion ($\xi > 0$), region I is associated with lower temperatures where dynamic restoration is limited, whereas region II coincides with the modestly elevated m-values and the plateau-type flow response at low strain rates (Fig. S1), consistent with DRV-assisted steady flow and limited DRX. Accordingly, region II provides the most relevant parameter space for applying large plastic strain in coarse-grained 4N Mg using low-ram-speed hot extrusion.

The macroscopic morphology after hot compression (Fig. 4(f)) corroborates the instability predictions: pronounced shear deformation and cracking are observed under conditions located in the unstable domains (e.g., 150 °C at

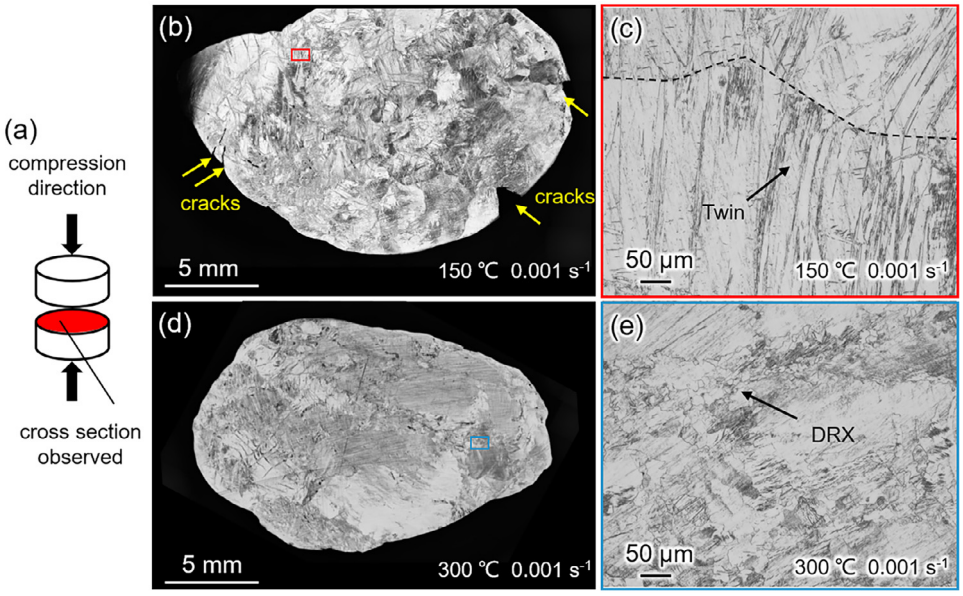


Fig. 5. The metallographic microstructure of cross section of hot compressed samples. (a) Schematic of the sampling method. (b–c) Results from the sample compressed under 150 °C and 0.001 s^{-1}. (d–e) Results from the sample compressed under 300 °C and 0.001 s^{-1}.

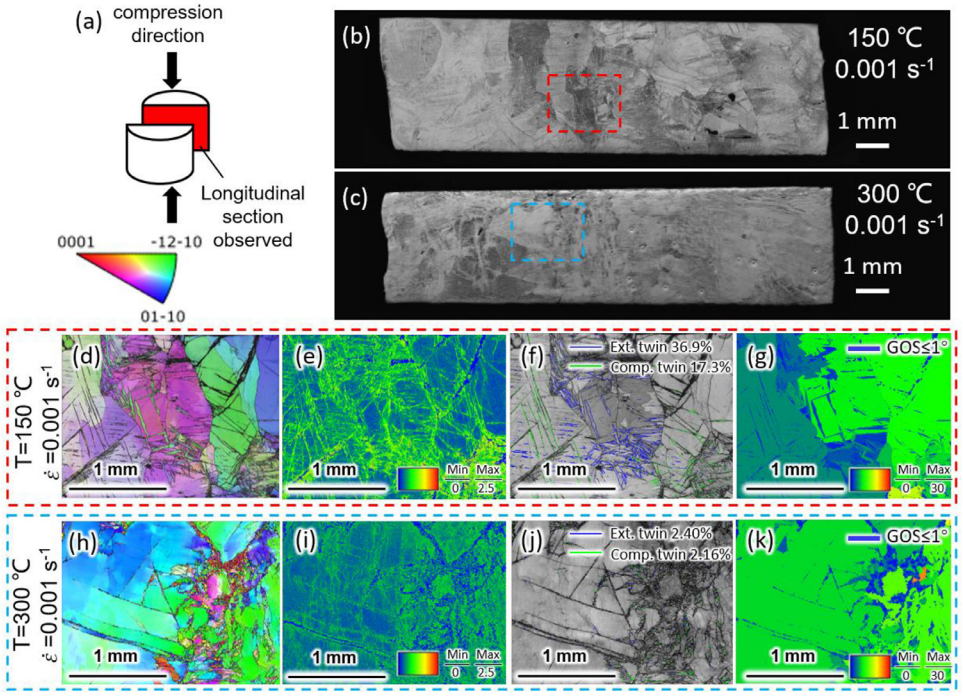


Fig. 6. Metallographic microstructure at longitudinal section of hot compressed samples. (a) Schematic of the sampling method. (b) and (c) are longitudinal section morphology after hot compression at 150 °C/0.001 s^{-1} and at 300 °C/0.001 s^{-1}, respectively. (d–g) EBSD characterization of the selected region in (b): (d) inverse pole figure (IPF) map, (e) kernel average misorientation (KAM) map, (f) special grain-boundary map showing extension and compression twins, and (g) grain orientation spread (GOS) map. (h–k) EBSD characterization of the selected region in (c): (h) IPF map, (i) KAM map, (j) special grain-boundary map showing extension and compression twins, and (k) GOS map.

0.001 s^{-1} and 300 °C at 0.1–1 s^{-1}), whereas samples deformed within the stable domains show more homogeneous barreling. Guided by these maps, we selected 150 °C/0.001 s^{-1} (twinning-dominated, unstable) and 300 °C/0.001 s^{-1} (stable, DRV/DRX-assisted) as representative conditions for microstructural analysis (Figs. 5 and 6).

3.2. Microstructure of Mg inside and outside the processing window

Fig. 5 shows the cross-sectional microstructures of high-purity Mg after two representative hot compression conditions (150 °C/0.001 s^{-1} and 300 °C/0.001 s^{-1}). Results for the sam-

ple compressed at 150 °C/0.001 s^{-1} are shown in Fig. 5 (b and c). The deformed grain size remains similar to that of the undeformed sample (Fig. 1(a)), approximately ~1 to 2 mm, with most grains being equiaxed. Twins are distributed throughout the majority of these grains, with the twin lamellae having a thickness of approximately 2–5 μm, as observed under high magnification (Fig. 5(c)). Macroscopic cracks (indicated by yellow arrows in Fig. 5(b)) are observed along the grain boundaries, with crack lengths ranging from 200 to 500 μm. These cracks are likely attributed to stress concentration at the grain boundaries, where the material is more prone to failure, particularly in larger grains. The cracks are predominantly located at the edges of the compressed samples, where the strain is higher than in the interior, resulting in increased stress concentration. Furthermore, the interaction of twins may have contributed to localized stress concentrations, leading to brittle cracking along the twin boundaries. This is consistent with the higher flow-stress characteristics exhibited by the stress-strain curves under this condition (Fig. S1(d)). Under the compression conditions of 300 °C/0.001 s^{-1}, the microstructure of the sample shows the coexistence of recrystallized fine grains and coarser grains, reflecting a complex dynamic recrystallization (DRX) behavior. Larger grains, with sizes up to ~5 mm, are observed in some regions, indicating grain growth (Fig. 5(d)). In contrast, recrystallized grains, predominantly located at the grain boundaries, are notably finer, with sizes ranging from 10 to 20 μm (Fig. 5(e)), indicating DRX in these regions.

Fig. 6 shows the longitudinal section microstructures of high-purity Mg after compression at 150 °C, 0.001 s^{-1} and 300 °C, 0.001 s^{-1}, together with EBSD analysis. For the sample compressed at 150 °C/0.001 s^{-1}, the longitudinal-section metallographic image (Fig. 6(b)) shows coarse grains with a characteristic size of ~2 mm, similar to the initial as-cast microstructure (Fig. 1). The IPF map of the selected region (Fig. 6(d)) further reveals abundant twins within the coarse grains, most of which are inclined at approximately 45° to the compression axis. According to the KAM (Kernel Average Misorientation) results (Fig. 6(e)), elevated local misorientation near twin boundaries indicates localized strain partitioning caused by deformation incompatibility between the twin and matrix. Such heterogeneity may promote local stress concentration and crack initiation during further deformation. Subsequently, the types of twins generated during compression were analyzed. As shown in Fig. 6(f), the coarse-grained Mg primarily forms tensile twins and compression twins under compressive loading, accounting for 36.9% and 17.3% respectively. Among the compression twins, the D38 type dominates (12.1%), accompanied by a minor fraction of D30 twins (3.26%) as well as others. According to previous studies [58], the D38-dominated twin structure promotes intense strain localization, creating preferential sites for micro-void nucleation and crack propagation along twin boundaries and the non-Schmid behavior of secondary twins associated with D38 variants results in heterogeneous deformation and reduced work hardening capacity, ultimately degrading the mechanical performance. Fig. 6(g) shows the grain orientation spread (GOS) map of the 150 °C sample, where most grains exhibit elevated GOS values and only limited regions show low GOS. These features indicate that deformation at 150 °C is mainly accommodated by twinning, accompanied by strong local strain heterogeneity.

At 300 °C, 0.001 s^{-1} (Fig. 6(c)), the longitudinal-section microstructure remains heterogeneous, with coarse deformed grains coexisting with fine grains near grain boundaries and twin boundaries. In contrast to the 150 °C sample, EBSD analysis shows markedly reduced twin fractions, lower KAM values in fine-grained regions and a more pronounced population of low-GOS grains. These features are consistent with enhanced dynamic recovery and partial dynamic recrystallization during hot compression. Therefore, deformation at 300 °C is no longer dominated by extensive twinning, but is increasingly accommodated by DRV/DRX-assisted flow. This interpretation agrees with the stable processing domain identified from the processing map.

Fig. 6(h–k) provides EBSD evidence for this deformation transition in the 300 °C sample. The IPF map shows fine grains distributed near grain boundaries and twin boundaries, while the KAM map reveals relatively low local misorientation in these fine-grained regions. The special grain-boundary map shows that the fractions of extension and compression twins decrease to 2.40% and 2.16%, respectively, much lower than those in the 150 °C sample. The GOS map further shows a higher population of low-GOS grains, supporting the occurrence of local recrystallization rather than extensive twinning-dominated deformation.

3.3. Constitutive equation for high-purity Mg

The constitutive relationship among flow stress, deformation temperature, and strain rate during isothermal deformation was described using the Sellars–Tegart hyperbolic sine model [59]:

$$\dot{\varepsilon} = A[\sinh(\alpha\sigma)]^n \exp\left(-\frac{Q}{RT}\right) \tag{7}$$

where ε is the strain rate, σ is the flow stress, T is the absolute temperature, R is the gas constant and A, n, α and Q are material constants. The corresponding low- and high-stress approximations, as well as the detailed derivation procedure, are provided in the Supplementary Information (S2).

To account for the combined effects of temperature and strain rate, the Zener–Hollomon parameter was employed [60]:

$$Z = \dot{\varepsilon} \exp\left(\frac{Q}{RT}\right) \tag{8}$$

Material constants were determined by linear regression of the experimental data. Specifically, the stress sensitivity parameters n and α were obtained from the fitted relationships between strain rate and flow stress (Fig. S2(a, b)). The activation energy Q was subsequently determined from the temperature dependence of the flow stress, yielding a value of 149.33 kJ·mol^{-1} (Fig. S2(c, d)).

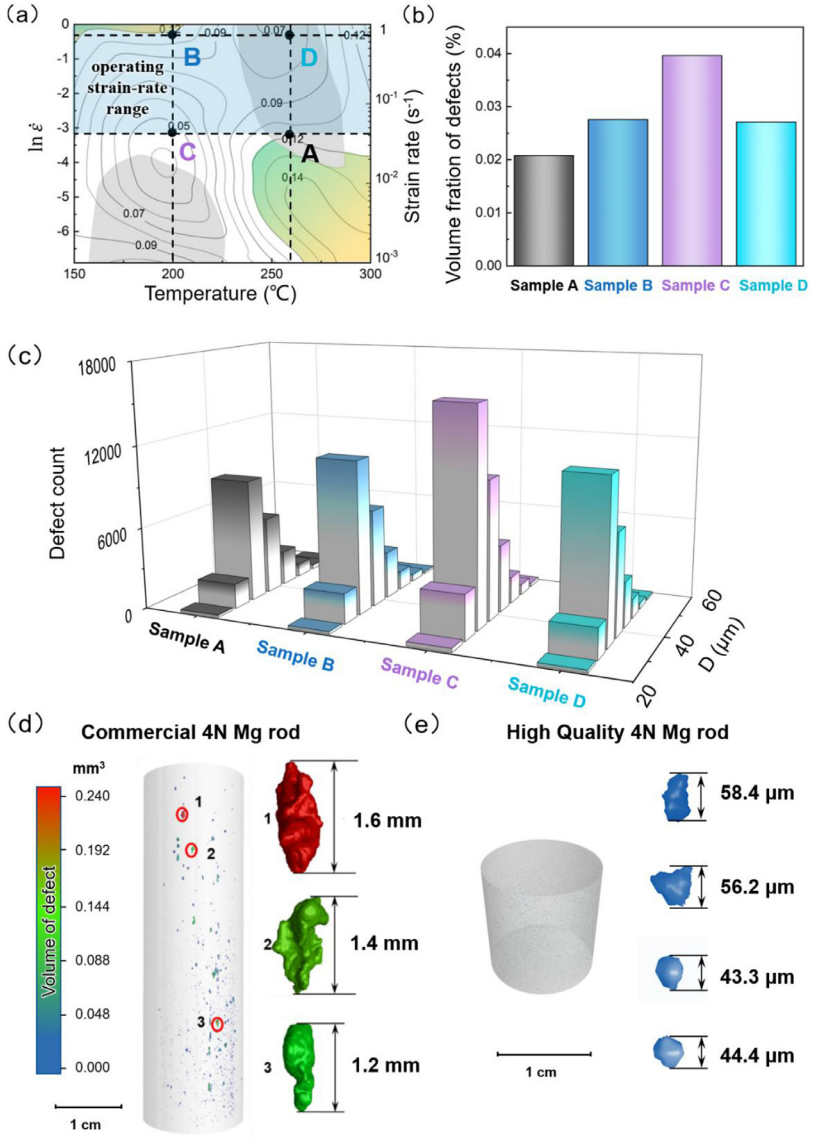


Fig. 7. CT inspection results of extruded rods under different extruding conditions. (a) The four extrusion parameters indicated in the processing map. The selected condition was chosen to approach the optimal processing window as closely as permitted by the available equipment. (b) Total volume fraction of internal defects of the extruded rods. (c) Count distribution of defects. (d) Morphology of defects in commercial pure Mg rod. (e) Morphology of defects in high quality 4N Mg rod processed via optimized extrusion parameters.

Using the determined parameters, the Z values under different deformation conditions were calculated, and linear fitting yielded $A = 2.131 \times 10^{13}$ and $n = 15.349$ (Fig. S2(e)). The linear relationship between $\ln Z$ and $\ln[\sinh(\alpha\sigma)]$ demonstrates a high correlation, with an R^2 value of 0.97, indicating the robustness of the fitting procedure. Accordingly, the constitutive equation for high-purity Mg can be expressed as:

$$\dot{\varepsilon} = 2.131 \times 10^{13}[\sinh(0.0165\sigma)]^{15.349} \times \exp\left(-\frac{149.33 \times 1000}{8.314T}\right) \quad (9)$$

3.4. Extrusion trials

The relationship between the mean effective strain rate and ram speed is given by the following equation [61]:

$$\dot{\bar{\varepsilon}} = \frac{6vD_C^2 \tan\alpha}{\left(D_C^3 - D_E^3\right)} 2\ln\frac{D_C}{D_E} \quad (10)$$

where v is the average ram speed, D_c is the diameter of container bore, D_E is the diameter of the extruded rod, and α is the semi-angle of dead-metal zone. In this study, $D_c = 105$ mm, $D_E = 10$ mm, $\alpha = 70°$.

Based on this relation, two processing windows and two non-processing windows were selected, and the corresponding extrusion parameters were calculated and applied (Fig. 7(a)). X-ray CT results (Fig. 7(b)), show that rods extruded under optimized conditions exhibit substantially lower defect content than those produced under non-optimal parameters. For sample A, the total defect volume fraction is reduced to 0.02%, corresponding to a 47.6% decrease relative to sam-

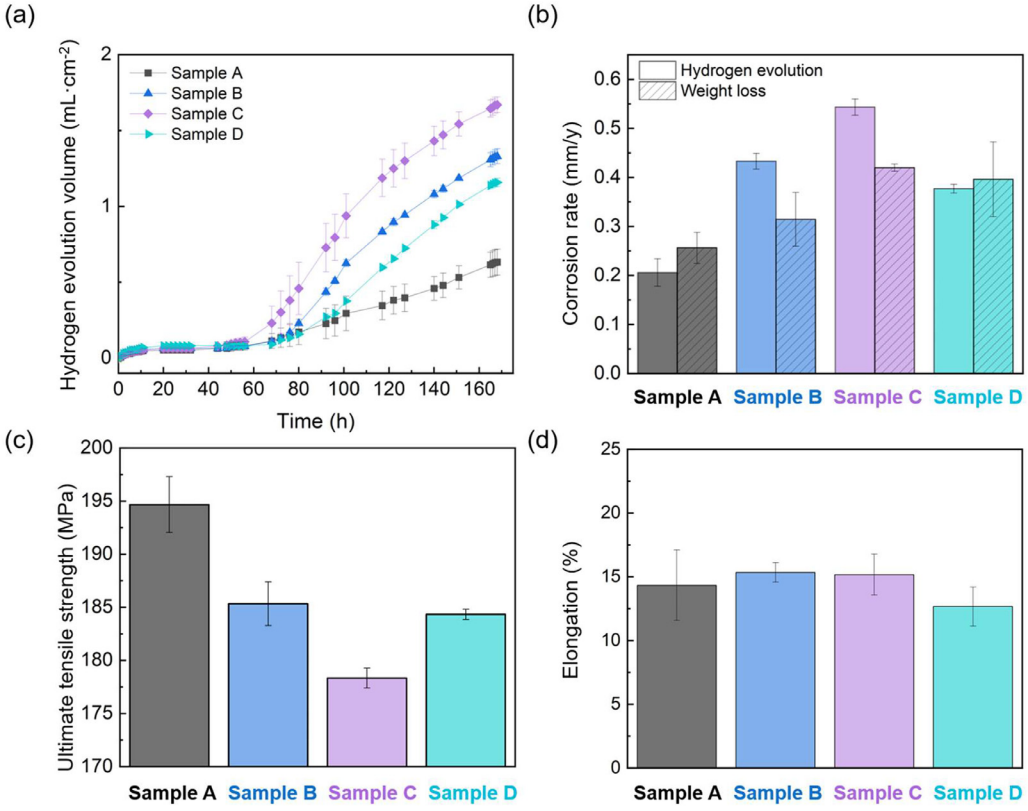


Fig. 8. Corrosion and mechanical properties of extruded high pure Mg rods. (a) Hydrogen evolution volume of the samples immersed in Hanks' solution. (b) Corrosion rates of the samples calculated by both hydrogen evolution and weight loss methods. (c) Ultimate tensile strength of the extruded rods. (d) Elongation of the extruded rods.

ple C, accompanied by a marked reduction in the absolute number of defects (Fig. 7(c)). In contrast, commercial pure Mg rods (Fig. 7(d)) contain defects larger than 1 mm that are widely distributed throughout the interior and predominantly non-spherical in shape. By comparison, rods produced using the optimized extrusion strategy contain no defects larger than ~60 μm—approximately two orders of magnitude smaller—with most defects exhibiting near-spherical morphologies (Fig. 7(e)). Additional large-area CT scans for processing windows I and II, together with the corresponding metallographic microstructures, are provided in Fig. S3.

The corrosion and mechanical properties of the extruded rods were evaluated, as summarized in Fig. 8. Hydrogen evolution was measured over time for all samples immersed in Hank's solution (Fig. 8(a)). Sample C showed the highest hydrogen evolution volume, with a consistent increase in volume over the testing period. Sample A exhibited the lowest hydrogen evolution, while Samples B and D showed intermediate values. Corrosion rates were determined via hydrogen evolution and weight loss methods (Fig. 8(b)). Both methods showed consistent results, with Sample C exhibiting the highest corrosion rate, followed by Sample B and Sample D. Sample A exhibited the lowest corrosion rate, indicating superior corrosion resistance, which is consistent with its reduced population of large and irregular defects (Fig. 7(e)). The ultimate tensile strength of the extruded rods was highest in Sample A at 195 MPa, followed by Sample B at approximately 185 MPa. Samples C and D exhibited similar tensile strengths, slightly lower than Sample B. Sample D demonstrated the highest elongation at fracture, surpassing 17%, followed by Samples C and B, which showed elongation values around 14%. Sample A exhibited the lowest elongation at fracture, just above 12%. Representative engineering stress–strain curves are shown in Fig. S4, and the tensile test results are compiled in Table S6.

4. Discussion

Extrusion conducted within the DRV/DRX-stable window restructures the defect population. X-ray CT shows that rods extruded from our billets exhibit an exceptionally low defect volume fraction (< 0.03%), with defects predominantly appearing as near-spherical 20–40 μm pores and only a limited tail approaching ~60 μm (Fig. 7(b)). In marked contrast, the examined commercial 4N Mg rod contains millimeter-scale defects, including shrinkage cavities and inclusion clusters extending along the extrusion direction (Fig. 7(d)). This difference in defect statistics cannot be explained by the purity of feedstock alone, it reflects a processing trajectory that promotes defect closure and spheroidization under stable plastic flow [62,63]. The simultaneous reduction in defect density and increase in defect sphericity also shift the dominant failure mode from defect-controlled to microstructure-controlled,

which further improved the mechanical performance of the extruded rods.

At the mechanistic level, defect attenuation requires the concurrent action of compressive triaxiality and deformation stability. Axisymmetric extrusion imposes a strongly negative mean stress in the billet core, favoring void closure by driving surrounding material into cavities and suppressing the tensile-triaxiality conditions needed for void growth and coalescence (porous-plasticity arguments) [64–66]. Importantly, compressive loading is necessary but not sufficient: when the flow field becomes unstable, shear localization and adiabatic softening can elongate pores and clusters into crack-like defects and promote shear cracking, thereby amplifying the structural penalty of inherited porosity. By operating within the DRV/DRX-stable regime, the low strain rate suppresses localization and extends the time available for climb/cross-slip-assisted recovery and limited recrystallisation, which relax stress concentrations and accommodate strain without catastrophic banding, enabling progressive pore collapse and suppressing extrusion-induced cracking. The dominance of equiaxed pores is therefore mechanistically informative: it signals a transition from notch-like cavities to curvature-minimized morphologies. Such rounding is consistent with capillarity-driven spheroidization at elevated temperature, with kinetics facilitated by deformation-generated short-circuit transport along dislocations and sub-grain boundaries formed during DRV/incipient DRX [67,68].

This defect-topology transition provides a direct route to the observed $>$ 190 MPa tensile strength (195 MPa for Sample A) without invoking precipitation or solute strengthening. Once millimeter-scale cavities and inclusion clusters are removed, fracture is no longer dictated by a small number of dominant internal notches; instead, the attainable strength approaches that set by the deformation substructure. Truncating the upper tail of the defect-size distribution increases the stress required for unstable cracking via a largest-flaw criterion (Griffith/LEFM-type scaling for crack-like defects, $\sigma \propto 1/\sqrt{a}$) and, equivalently, lowers the probability of sampling a critical flaw within the gauge length (statistical-strength/Weibull arguments) [69–71]. With this extrinsic limitation relaxed, intrinsic strengthening mechanisms introduced during stable hot working become decisive. In the identified domain—characterized by non-basal slip participation and recovery/recrystallisation mediated by cross-slip and climb—deformation is expected to generate a dense hierarchy of sub-boundaries and recrystallized interfaces (consistent with EBSD evidence for DRX nucleation at grain and twin boundaries), which increases boundary-mediated slip resistance (Hall–Petch-type contribution) while retained dislocations provide forest hardening (Taylor-type) [72,73]. In addition, extrusion texture can elevate the macroscopic flow stress along the extrusion axis by biasing deformation away from easy basal slip, thereby increasing the effective resistance to plastic flow in tension [74–75]. Together, these mechanisms offer an explanation for why a high-purity Mg system can nonetheless sustain high strength once the governing defect scale is suppressed.

The differences in degradation rate among the extruded rods are governed primarily by defect topology, with corrosion-product layer continuity and deformation heterogeneity further modulating defect-driven localized degradation [76,77]. Sample A, extruded within the DRV/DRX-stable domain, contains fewer large, irregular and clustered defects and therefore exhibits the lowest hydrogen evolution and weight-loss corrosion rate. Large non-spherical pores and inclusion clusters are particularly detrimental because they provide crevice-like geometries, defect–matrix interfaces and local electrochemical heterogeneity, which serve as preferential initiation sites for localized corrosion [78,79]. Once corrosion initiates at these sites, local geometry and electrochemical heterogeneity can hinder the formation of a continuous corrosion-product layer, leading to repeated film rupture, weakened barrier protection and sustained localized degradation [80–82]. Consistent with this interpretation, post-immersion SEM observations after 7 d in Hank's solution show a comparatively uniform corrosion-product layer on Sample A, whereas Samples B–D exhibit more pronounced pitting and local rupture of the corrosion-product layer (Fig. S5). Besides defect topology, extrusion outside the stable flow regime may promote heterogeneous deformation, twinning and strain localization, which can further destabilize the early corrosion-product layer [83–86]. Thus, we suggest that the improved degradation resistance of Sample A is primarily associated with defect suppression, with possible contributions from more stable corrosion-product layer development and reduced microstructural heterogeneity.

5. Summary and conclusion

High-purity Mg is attractive for biodegradable implants, but its translation is limited by the combination of poor hot workability and casting-derived defects that simultaneously undermine strength and accelerate localized degradation. Here we show that these barriers can be overcome by coupling impurity-controlled, closed-atmosphere melting with controlled thin-layer solidification casting (CTLSC) and by selecting a DRV/DRX-stable deformation pathway guided by processing maps and constitutive analysis. Hot-compression data reveal that coarse-grained 4N Mg exhibits persistently low strain-rate sensitivity (m = 0.03–0.08) and low power-dissipation efficiency ($\eta \leq \sim$0.15), indicating a fundamentally narrow processing window in which microstructural evolution is limited and flow instability must be actively avoided; within this window, the dominant deformation mode transitions from twinning at lower temperatures to DRV/DRX-assisted flow at higher temperatures under low strain rates. Extrusion validation demonstrates that extrusion inside the DRV/DRX-stable domain drives defect collapse and spheroidization rather than relying on extensive grain refinement, reducing the maximum defect size to $<$ 60 μm and lowering the total defect volume fraction to $<$ 0.03%, in contrast to the examined commercial rod, which contains millimeter-scale cavities. This defect-controlled state translates into a tensile strength of ∼195 MPa together with a low *in vitro* degradation rate (∼0.2 mm·y^{-1}

in Hank's solution), evidencing that mechanical integrity and corrosion control can be achieved concurrently in high-purity Mg.

More broadly, this study establishes a practical framework linking processing, structure, and defect management in high-purity Mg. By focusing on defect engineering, it provides a practical approach to ensuring the quality of Mg feedstocks, especially for small biomedical devices where even a single critical flaw could affect reliability. The present study focuses on extrusion processing, defect suppression and short-term *in vitro* degradation of 4N Mg rods. Further long-term *in vitro* testing, *in vivo* evaluation and device-specific validation will be required before clinical translation.

Declaration of generative AI and AI-assisted technologies in the writing process

During the preparation of this manuscript, the authors utilized ChatGPT solely to refine linguistic precision and ensure grammatical accuracy. All conceptual frameworks, mechanistic analyses, and original drafts were developed independently by the authors. The final content has been carefully reviewed and edited by the authors, who maintain full responsibility for the scientific integrity and veracity of the publication.

Data availability

The data that support the findings of this study are available from the corresponding authors upon reasonable request.

Declaration of competing interest

The author is an Editorial Board Member/Editor-in-Chief/Associate Editor/Guest Editor for this journal and was not involved in the editorial review or the decision to publish this article. Zhiwei Shan is an editorial board member for Journal of Magnesium and Alloys and was not involved in the editorial review or the decision to publish this article. All authors declare that there are no competing interests.

CRediT authorship contribution statement

Weichao Li: Writing – review & editing, Writing – original draft, Investigation, Formal analysis. **Degang Xie:** Writing – review & editing, Supervision, Project administration, Funding acquisition, Conceptualization. **Tingjiang Pan:** Writing – review & editing, Formal analysis. **Chuanwei Fan:** Writing – review & editing, Resources. **Fengge Xi:** Writing – review & editing, Formal analysis. **Yuanhao Jia:** Writing – review & editing. **Zhiwei Shan:** Writing – review & editing, Supervision, Project administration, Funding acquisition, Conceptualization.

Acknowledgment

The authors acknowledge the support of the National Natural Science Foundation of China (Grant No U24A2021, Grant No 52522103 and Grant No 52371122), the Science and Technology Departments of Shaanxi Province, China (Grant No 2023GXLH-029), Shaanxi Province Foundation for Distinguished Young Scholars (Grant No 2024JC-JCQN-47), and the Science and Technology Bureau of Yulin, Shaanxi, China (Grant No 2023-CXY-199). We thank Shaanxi Guoke Magnesium Industry Technology Co., Ltd. for providing the high-purity raw materials, and to its engineering team for their valuable assistance in the plastic forming process.

Supplementary materials

Supplementary material associated with this article can be found, in the online version, at doi:10.1016/j.jma.2026.102189.

References

[1] F.Z. Akbarzadeh, M. Sarraf, E.R. Ghomi, et al., J. Magnes. Alloys 12 (2024) 2569–2594.
[2] V. Herber, B. Okutan, G. Antonoglou, et al., J. Clin. Med. 10 (2021) 1842.
[3] R. Davis, A. Singh, M.J. Jackson, et al., Int. J. Adv. Manuf. Technol. 120 (2022) 1473–1530.
[4] S.M. Zielinski, M.J. Heetveld, M. Bhandari, et al., J. Orthop. Trauma 29 (2015) e285–e292.
[5] T. Zhang, W. Wang, J. Liu, et al., Front. Bioeng. Biotechnol. 10 (2022) 953344.
[6] J. Bennett, Q. De Hemptinne, K. McCutcheon, et al., Expert Rev. Med. Devices 16 (2019) 757–769.
[7] P. Rider, Ž.P. Kačarević, A. Elad, et al., Bioact. Mater. 14 (2022) 152–168.
[8] National Medical Products Administration, Biodegradable Magnesium Metal Closure Clamp Approved For Market Launch, https://www.nmpa.gov.cn/zhuanti/ypqxgg/gggzjzh/20231215142805123.html (Accessed December, 15 2023).
[9] Y.D. Li, W.R. Li, Y.L. Hua, F.F. Liu, A kind of degradable synthetism stick implantation instrument and preparation method thereof, Chinese Patent CN108744058A, 2018.
[10] Y.J. Cao, X. Wang, X.Q. Wang, H.D. Xu, A degradable bone screw for promoting fracture surface healing and preparation method thereof, Chinese Patent CN118000877A, 2024.
[11] Wuxi Second People's Hospital, method for manufacturing degradable inorganic hernia patch, Chinese Patent CN116370138A, 2023.
[12] L. Chang, Y. Luo, W. Li, et al., Regen. Biomater. 11 (2024) rbae095.
[13] S. Huang, B. Wang, X. Zhang, et al., Biomaterials 238 (2020) 119829.
[14] D.W. Zhao, T.W. Zhang, W.D. Wang, et al., J. Orthop. Transl. 51 (2025) 198–206.
[15] H. Wu, C. Zhang, T. Lou, et al., Acta Biomater. 98 (2019) 152–159.
[16] Y. Huang, J. Li, F. Lian, et al., Biodegradable magnesium alloy biological implant material for bone nail, bone plate, and cardiovascular bracket contains zinc, calcium, iron, nickel, copper, and magnesium, Chinese Patent CN104498790A, 2015.
[17] X.H. Feng, H.M. Jia, Y.T. Liu, et al., Mater. Sci. Forum 849 (2016) 114–120.
[18] Y.Q. Li, F. Li, F.W. Kang, et al., J. Alloys Compd. 953 (2023) 170080.
[19] J. Hofstetter, E. Martinelli, A.M. Weinberg, et al., Corros. Sci. 91 (2015) 29–36.
[20] B. Sui, H. Lu, X. Liu, et al., J. Mater. Sci. Technol. 140 (2023) 58–66.
[21] J. Chen, J. Dai, J. Qian, et al., Materials (Basel) 15 (2022) 3991.
[22] S. Johnston, Z. Shi, A. Atrens, Corros. Sci. 101 (2015) 182–192.
[23] Chinese Society for Biomaterials, Medical high purity magnesium extruded round bar: T/CSBM 0041–2023, 2023. Available at: https://www.csbm.org.cn/download/20230426105131.pdf. (Accessed April 24, 2023).

[24] S. Zhang, X. Zhang, C. Zhao, et al., Acta Biomater. 6 (2010) 626–640.
[25] S. El-Rahman, Pharmacol. Res. 47 (2003) 189–194.
[26] J.L. Zhang, S.B. Wang, M.Z. Li, et al., Mater. Sci. Forum 546–549 (2007) 195–198.
[27] K. Zhu, J. Wang, W. Zhang, et al., Trans. Nonferrous Met. Soc. China 34 (2024) 423–434.
[28] J. Gu, M. Gao, S. Yang, et al., Mater. Des. 186 (2020) 108357.
[29] S.P. Zhu, Y. Ai, D. Liao, et al., Int. J. Fract. 234 (2022) 21–43.
[30] K. Thekkepat, H.S. Han, J.W. Choi, et al., J. Magnes. Alloys 10 (2022) 1972–1980, doi:10.1016/j.jma.2021.06.019.
[31] F. Witte, Acta Biomater. 6 (2010) 1680–1692.
[32] K.S. Kim, J.C. Park, C.D. Yim, et al., Procedia Eng. 10 (2011) 165–170.
[33] M.F. Horstemeyer, N. Yang, K. Gall, et al., Fatigue Fract. Eng. Mater. Struct. 25 (2002) 1045–1056, doi:10.1046/j.1460-2695.2002.00594.x.
[34] K.X. Kuah, D.J. Blackwood, W.K. Ong, M. Salehi, H.L. Seet, M.L.S. Nai, S. Wijesinghe, J. Magnes. Alloys 10 (2022) 1296–1310, doi:10.1016/j.jma.2021.11.016.
[35] M.C.L. de Oliveira, R.M.P. da Silva, R.M. Souto, R.A. Antunes, J. Magnes. Alloys 12 (2024) 3062–3093, doi:10.1016/j.jma.2024.07.030.
[36] P. Zhao, T. Ying, F. Cao, X. Zeng, W. Ding, J. Magnes. Alloys 11 (2023) 3120–3129, doi:10.1016/j.jma.2021.09.003.
[37] S.L. Sin, A. Elsayed, C. Ravindran, Int. Mater. Rev. 58 (2013) 419–436.
[38] A. Bahmani, S. Arthanari, K.S. Shin, J. Magnes. Alloys 8 (2020) 134–149, doi:10.1016/j.jma.2019.12.001.
[39] R. Zheng, B. Yang, W.C. Li, Z.H. Qiang, B.Y. Liu, Z.W. Shan, Magnesium Technology 2025. TMS 2025. The Minerals, Metals & Materials Series, D. Tolnai, A. Palumbo, A. Leonard, N.R. Neelameggham (Eds.), Springer, Cham, 2025, doi:10.1007/978-3-031-81061-9_13.
[40] E. Karakulak, J. Magnes. Alloys 7 (2019) 355–369, doi:10.1016/j.jma.2019.05.001.
[41] A.P. Carvalho, R.B. Figueiredo, Mater. Trans. 64 (2023) 1272–1283.
[42] I. Serrano-Munoz, J.Y. Buffiere, R. Mokso, et al., Sci. Rep. 7 (2017) 45239.
[43] P. Bakke, P.K. Andersen, J.M. Svalestuen, et al., Mater. Sci. Forum 488–489 (2005) 65–72.
[44] Z. Li, J. Zhang, S. Liu, et al., J. Rare Earths 42 (2024) 2350–2361.
[45] Y. Zheng, Y. Zhang, Y. Liu, et al., Materials (Basel) 16 (2023) 3791.
[46] X.Y. Peng, D.G. Xie, L.Q. Bai, et al., J. Magnes. Alloys 13 (2025) 5393–5403, doi:10.1016/j.jma.2024.10.018.
[47] Z. Zeng, N. Stanford, C.H.J. Davies, et al., Int. Mater. Rev. 64 (2019) 27–62.
[48] H. Wang, X.C. Luo, D.T. Zhang, et al., J. Mater. Sci. Technol. 199 (2024) 27–52.
[49] X. Xia, K. Zhang, M. Ma, T. Li, J. Magnes. Alloys 8 (2020) 917–928, doi:10.1016/j.jma.2020.02.018.
[50] Z. Zeng, J.F. Nie, S.W. Xu, et al., Nat. Commun. 8 (2017) 972.
[51] F. Ueberschär, K. Kittner, M. Ullmann, et al., Prod. Eng. 19 (2025) 543–558.
[52] Z.W. Shan, R. Zheng, B. Yang, L.Y. Mao, W.C. Li, Magnesium and magnesium alloy casting device and method based on melt controlled-speed drop casting, Chinese Patent CN114247857B, 2022.
[53] Y.V.R.K. Prasad, Hot Working Guide: A Compendium of Processing Maps, K.P. Rao, S. Sasidhara (Eds.), ASM International, Materials Park, OH, 2015.
[54] M.R. Barnett, Mater. Sci. Eng. A 464 (2007) 1–7.
[55] Y.V.R.K. Prasad, T. Seshacharyulu, Int. Mater. Rev. 43 (1998) 243–258, doi:10.1179/imr.1998.43.6.243.
[56] R. Raj, Met. Trans. A 12 (1981) 1089–1097, doi:10.1007/BF02643490.
[57] S.C. Sutton, A.A. Luo, J. Magnes. Alloys 8 (2020) 111–126, doi:10.1016/j.jma.2019.11.007.
[58] B. Yang, J. Wang, Y. Li, et al., Scr. Mater. 235 (2023) 115620, doi:10.1016/j.scriptamat.2023.115620.
[59] C.M. Sellars, W.J. McG, Met. Rev. 17 (1972) 1–24, doi:10.1179/imtlr.1972.17.1.1.
[60] C. Zener, J.H. Hollomon, J. Appl. Phys. 15 (1944) 22–32, doi:10.1063/1.1707363.
[61] P.K. Saha, Aluminum Extrusion Technology, ASM International, Materials Park, OH, 2000.
[62] P. Wan, J.F. Tang, C.F. Gao, in: Proceedings of the 2017 Symposium on Piezoelectricity, Acoustic Waves, and Device Applications, Chengdu, IEEE, 2017, pp. 336–339, doi:10.1109/SPAWDA.2017.8340352.
[63] K.R. Kashyzadeh, N. Amiri, E. Maleki, et al., J. Mar. Sci. Eng. 11 (2023) 527, doi:10.3390/jmse11030527.
[64] A.L. Gurson, J. Eng. Mater. Technol. 99 (1977) 2–15, doi:10.1115/1.3443401.
[65] J.R. Rice, D.M. Tracey, J. Mech. Phys. Solids 17 (1969) 201–217, doi:10.1016/0022-5096(69)90033-7.
[66] M. Saby, P.O. Bouchard, M. Bernacki, J. Manuf. Process. 19 (2015) 239–250, doi:10.1016/j.jmapro.2014.05.006.
[67] G.R. Love, Acta Metall. 12 (1964) 731–737, doi:10.1016/0001-6160(64)90220-2.
[68] R.L. Coble, J. Appl. Phys. 32 (1961) 787–792, doi:10.1063/1.1736107.
[69] W. Weibull, J. Appl. Mech. 18 (1951) 293–297, doi:10.1115/1.4010337.
[70] G.R. Irwin, J. Appl. Mech. 24 (1957) 361–364, doi:10.1115/1.4011547.
[71] A.A. Griffith, Philos. Trans. R. Soc. A 221 (1921) 163–198, doi:10.1098/rsta.1921.0006.
[72] H. Yu, Y. Xin, M. Wang, Q. Liu, J. Mater. Sci. Technol. 34 (2018) 248–256, doi:10.1016/j.jmst.2017.07.022.
[73] D. Hull, D.J. Bacon, Introduction to Dislocations, 5th ed., Elsevier, Oxford, 2011.
[74] N.E. Stanford, K. Sotoudeh, P.S. Bate, Acta Mater. 59 (2011) 4866–4874, doi:10.1016/j.actamat.2011.04.028.
[75] W.K. Wang, W.Z. Xie, T.T. Kang, et al., J. Magnes. Alloys 13 (2025) 4259–4277, doi:10.1016/j.jma.2024.03.005.
[76] G.L. Song, A. Atrens, J. Magnes. Alloys 11 (2023) 3948–3991, doi:10.1016/j.jma.2023.08.012.
[77] M. Esmaily, J.E. Svensson, S. Fajardo, et al., Prog. Mater. Sci. 89 (2017) 92–193, doi:10.1016/j.pmatsci.2017.04.011.
[78] K.X. Kuah, M. Salehi, W.K. Ong, et al., NPJ Mater. Degrad. 6 (2022) 36, doi:10.1038/s41529-022-00244-2.
[79] F. Cao, Z. Shi, G.L. Song, et al., Corros. Sci. 94 (2015) 255–269, doi:10.1016/j.corsci.2015.02.002.
[80] A. Atrens, G.L. Song, F. Cao, et al., J. Magnes. Alloys 1 (2013) 177–200, doi:10.1016/j.jma.2013.09.003.
[81] C. Taltavull, Z. Shi, B. Torres, J. Rams, A. Atrens, J. Mater. Sci. Mater. Med. 25 (2014) 329–345, doi:10.1007/s10856-013-5087-y.
[82] G.L. Song, K.A. Unocic, Corros. Sci. 98 (2015) 758–765, doi:10.1016/j.corsci.2015.05.047.
[83] J. Huang, G.L. Song, Y. Zhu, D. Zheng, Z. Wang, J. Magnes. Alloys 11 (2023) 230–248, doi:10.1016/j.jma.2021.05.008.
[84] A. Atrens, Z. Shi, S.U. Mehreen, S. Johnston, G.L. Song, X. Chen, F. Pan, J. Magnes. Alloys 8 (2020) 989–998, doi:10.1016/j.jma.2020.08.002.
[85] Y. Yang, F. Scenini, M. Curioni, Electrochim. Acta 198 (2016) 174–184, doi:10.1016/j.electacta.2016.03.043.
[86] L. Wang, Y. Lu, H. Chai, et al., Mater. Today Commun. 32 (2022) 104065, doi:10.1016/j.mtcomm.2022.104065.